Journal of High Energy Physics, Gravitation and Cosmology, 2024, 10, 8-26
https://www.scirp.org/journal/jhepgc
ISSN Online: 2380-4335
ISSN Print: 2380-4327

Classical Cosmology I. Anomalous Redshift for Galaxies in NED-D

Lorenzo Zaninetti

Physics Department, University of Turin, Turin, Italy
Email: l.zaninetti@alice.it

How to cite this paper: Zaninetti, L. (2024) Classical Cosmology I. Anomalous Redshift for Galaxies in NED-D. *Journal of High Energy Physics, Gravitation and Cosmology*, **10**, 8-26.
https://doi.org/10.4236/jhepgc.2024.101002

Received: August 31, 2023
Accepted: January 5, 2024
Published: January 8, 2024

Abstract

Three mechanisms for an alternative to the Doppler effect as an explanation for the redshift are reviewed. A fourth mechanism is the attenuation of the light as given by the Beer-Lambert law. The average value of the Hubble constant is therefore derived by processing the galaxies of the NED-D catalog in which the distances are independent of the redshift. The observed anisotropy of the Hubble constant is reproduced by adopting a rim model, a chord model, and both 2D and 3D Voronoi diagrams.

Keywords

Galaxy Groups, Clusters, Superclusters, Large Scale Structure of the Universe Cosmology

1. Introduction

In the recent literature, the Hubble constant has been oscillating between a low value, as determined by the Planck collaboration [1], $H_0 = (67.4 \pm 0.5)\,\mathrm{km \cdot s^{-1} \cdot Mpc^{-1}}$, and an high value, $H_0 = (74.03 \pm 1.42)\,\mathrm{km \cdot s^{-1} \cdot Mpc^{-1}}$, as measured on 70 long-period Cepheids in the Large Magellanic Cloud (LMC) [2]. This difference is referred to as the Hubble constant tension and the weighted mean is $H_0 = (70.53 \pm 4.94)\,\mathrm{km \cdot s^{-1} \cdot Mpc^{-1}}$. The source of the Hubble constant tension is a current field of research. We report some approaches among others. A model-independent principal component analysis (PCA) was carried out using an eigenmode decomposition of the varying constant during recombination [3], a color correction in the calibration sample for observations of Type Ia supernovae (SNe) and Cepheids [4], and a geometric mismatch in the comparison of the measurements which is equal to the temporal diameter of the surface of last scattering [5]. Another interesting topic is the anisotropy in the Hubble constant, which was predicted starting in 1975 [6] [7] [8]. A detailed analysis of the anisotropy in the Hubble constant has been done by a comparison of the constant in the North and South Galactic hemispheres [9] and by contour maps of the constant in Galactic coordinates [10]. These analyses introduce some doubts on the current status of the standard cosmology, see [11] for the status of the tired light cosmology in the period 1929-1939. Therefore the following questions can be posed:

1) Is the Hubble constant an universal constant or is it a measure of the absorption of light in the intergalactic medium?

2) What are the known physical mechanisms which produce the attenuation of the light?

3) Can we build some models for the anisotropy of the anomalous redshift?

In order to answer these questions, Section 2 reviews the statistics of a line crossing the origin, analyses the attenuation of the light as given by the Beer-Lambert law, reviews three models for the anomalous redshift, and introduces the NED catalog for galaxies. Section 3 reviews the luminosity Schechter function for galaxies and the photometric maximum in the number of galaxies versus redshift with an application to the NED catalog. In order to explain the anisotropy of the Hubble constant, three simple models are introduced in Section 4 and a fourth model uses the Voronoi diagrams, see Section 5.

2. Preliminaries

This section reviews the least square fit of a line crossing the origin, the attenuation of light according to the Beer-Lambert law, some physical mechanisms for the anomalous redshift, and the NED catalog for galaxies.

2.1. A Line Crossing the Origin

A sequence of data x_i, y_i and uncertainty σ_i in the *i*th variable in the interval $[1, n]$ which presents a linear behaviour is processed assuming a straight line of the form

$$y(x;a,b) = a + bx, \tag{1}$$

where *a* and *b* are deduced by minimizing χ^2 defined as

$$\chi^2(a,b) = \sum_i^n \left(\frac{y_i - a - bx_i}{\sigma_i} \right)^2, \tag{2}$$

see Section 15.2 in [12]. In some cases, we are interested in a model without intercept, *i.e.* $a = 0$:

$$y(x;b) = bx. \tag{3}$$

In the absence of uncertainties, the values of *b* and its uncertainty, σ_b, are found by minimizing χ^2,

$$\chi^2(b) = \sum_i^n (y_i - bx_i)^2, \tag{4}$$

and are given by

$$b = \frac{\sum_{i=1}^{n} x_i y_i}{\sum_{i=1}^{n} x_i^2}, \tag{5a}$$

$$\sigma_b = \sqrt{\frac{\sum_{i=1}^{n} (y_i - bx_i)^2}{(n-1)\left(\sum_{i=1}^{n} x_i^2\right)}}. \tag{5b}$$

In the presence of uncertainties, the parameter b and its standard error σ_b can be determined by minimizing

$$\chi^2(b) = \sum_{i}^{n} \left(\frac{y_i - bx_i}{\sigma_i} \right)^2, \tag{6}$$

yielding the values

$$b = \frac{\sum_{i=1}^{n} \frac{x_i y_i}{\sigma_i^2}}{\sum_{i=1}^{n} \frac{x_i^2}{\sigma_i^2}}, \tag{7a}$$

$$\sigma_b = \sqrt{\frac{1}{\sum_{i=1}^{n} \frac{x_i^2}{\sigma_i^2}}}. \tag{7b}$$

A nonlinear regression of the type

$$\ln(1+z) = bx, \tag{8}$$

can be made linear with the transformation

$$z' = \ln(1+z), \tag{9}$$

which now produces a linear regression

$$z' = bx. \tag{10}$$

2.2. The Attenuation of Light

We assume that the frequency ν of a photon which travels through intergalactic space decreases according to the following ODE, called the Beer-Lambert law, after [11] [13] [14],

$$\frac{\mathrm{d}}{\mathrm{d}x}\nu(x) = -kn_e\nu(x), \tag{11}$$

where n_e is the number density of matter in $1/\mathrm{m}^3$ and k the attenuation coefficient in m^2. This ODE is solved while assuming the initial condition $\nu(0) = nu_0$

$$\nu(x) = \nu_0 \mathrm{e}^{-kn_e x}. \tag{12}$$

We now define the redshift as a function of the wavelength λ and the initial wavelength λ_0 by

$$z = \frac{\lambda - \lambda_0}{\lambda_0}. \tag{13}$$

Making use of

$$\nu\lambda = c, \tag{14}$$

where c is the speed of light, we obtain

$$z = \mathrm{e}^{kn_e x} - 1, \tag{15}$$

or

$$\ln(z+1) = kn_e x. \tag{16}$$

Taking a Taylor expansion around $z = 0$ gives

$$z = kn_e x, \tag{17}$$

and the expansion velocity, v, in the radial Doppler framework can be obtained by multiplying both sides by c,

$$v = kn_e xc. \tag{18}$$

This equation can be equated to Hubble's Law [15]

$$v = H_0 x \frac{\mathrm{km}}{\mathrm{Mpc}}, \tag{19}$$

which gives

$$H_0 = kn_e c. \tag{20}$$

This equation allows determining the product of the attenuation coefficient and the number density

$$kn_e = 7.567 \times 10^{-27} \left(\frac{H_0}{70}\right)\frac{1}{\mathrm{m}}. \tag{21}$$

2.3. The Anomalous Redshift

The *first* case to be analysed is a plasma effect. In the framework of photons which penetrate a hot, sparse electron plasma, it is possible to derive a formula for the redshift:

$$\ln(1+z) = 3.326 \times 10^{-25} \int_0^R n_e \mathrm{d}x + \frac{\gamma_i - \gamma_0}{\xi\omega}, \tag{22}$$

where γ_i is the initial photon width, γ_0 is the final photon width, ω is the photon frequency, ξ is an adjustment factor and n_e is the number of plasma electrons per cm^3, see Equation (20) of [16] or Equation (29) of [17]. The second term of Equation (22) is a small correction to the first term and therefore we have a simple expression for the plasma redshift (in the CGS system),

$$\ln(1+z) = 3.326 \times 10^{-25} \int_0^R n_e \mathrm{d}x. \tag{23}$$

The above logarithmic dependence is similar to that of the attenuation of light as represented by Formula (16). The average electron plasma number density, $\langle n_e \rangle$, as a function of the Hubble constant is

$$\langle n_e \rangle = 2.27492 \times 10^{-4} \left(\frac{H_0}{70} \right) \frac{1}{\text{cm}^3}, \tag{24}$$

and the Hubble constant

$$H_0 = 307701.8 \langle n_e \rangle \text{km} \cdot \text{s}^{-1} \cdot \text{Mpc}^{-1}, \tag{25}$$

where $\langle n_e \rangle$ is expressed in 1/cm^3.

The second case to be analysed is the New Tired Light (NTL) hypothesis which has equations

$$H_0 = \frac{2 n_e h r_e}{m_e}, \tag{26a}$$

$$z = \exp \frac{H_0 * d}{c} - 1 \tag{26b}$$

where n_e is the number density of matter, h is Planck's constant, r_e is the classical radius of the electron, m_e is the mass of the electron, c is the speed of light, d is the distance and H_0 is the Hubble constant; see Equations (13) and (14) in [18]. Also in this case we have a logarithmic dependence similar to that of the attenuation of light as represented by Formula (16). The average number density of matter in NTL is

$$\langle n_e \rangle = 0.55337 \left(\frac{H_0}{70} \right) \frac{1}{\text{m}^3}, \tag{27}$$

and the Hubble constant

$$H_0 = 126.49 \langle n_e \rangle \text{km} \cdot \text{s}^{-1} \cdot \text{Mpc}^{-1}, \tag{28}$$

with $\langle n_e \rangle$ expressed in 1/m^3. The *third* case is represented by the interaction of a low density electromagnetic wave with an electron, see equation at page 3 in [19], which in the SI system produces the following redshift

$$z = w \int_0^D n_e \text{d}s, \tag{29}$$

with

$$w = \frac{3 q_e^4 \mu_0}{512 \pi m_e^2} = 2.33 \times 10^{-30} \text{ m}^2, \tag{30}$$

where q_e is the charge of the electron, μ_0 is the magnetic permeability of the vacuum, and m_e is the mass of the electron. The average electron number density in the interaction of a low density electromagnetic wave with an electron is

$$\langle n_e \rangle = \frac{H_0}{cw}, \tag{31}$$

or, in numbers,

$$\langle n_e \rangle = 3235.5 \left(\frac{H_0}{70} \right) \frac{1}{\text{m}^3}, \tag{32}$$

and the Hubble constant is

$$H_0 = 0.021634 \langle n_e \rangle \text{km} \cdot \text{s}^{-1} \cdot \text{Mpc}^{-1}, \tag{33}$$

with $\langle n_e \rangle$ expressed in 1/m^3.

2.4. The NED-D Catalog

The NASA/IPAC Extragalactic Database of Distances (NED-D) contains an estimate of the redshift versus an independent distance for 11,699 galaxies, see **Figure 1**. **Figure 2** reports the redshift against distance for the above catalog and the connecting line with uncertainty which allows the determination of H_0, $\langle n_e \rangle$ and kn_e. The cosmological results are shown in **Table 1** for a straight line with and without uncertainty.

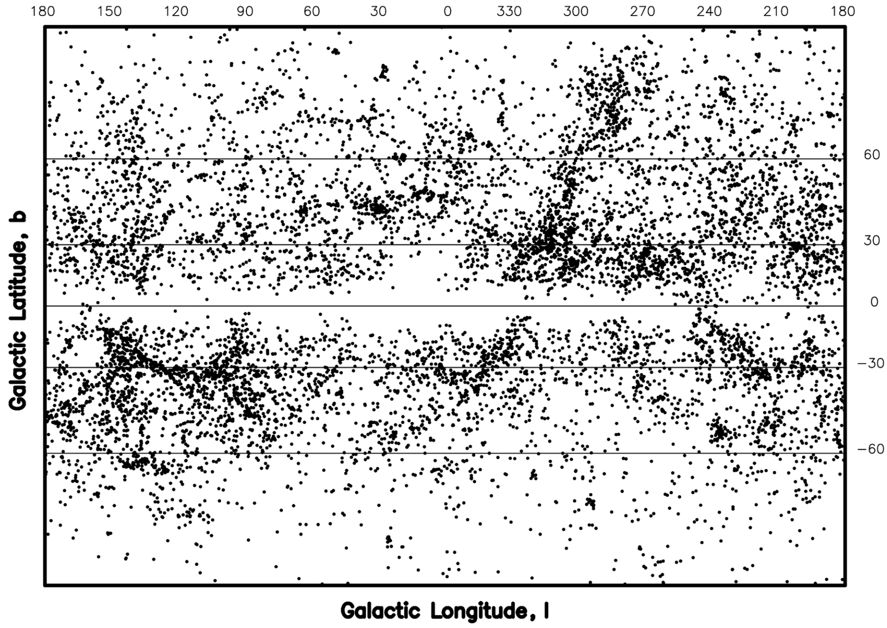

Figure 1. Mercator projection in galactic coordinates of the NED's galaxies.

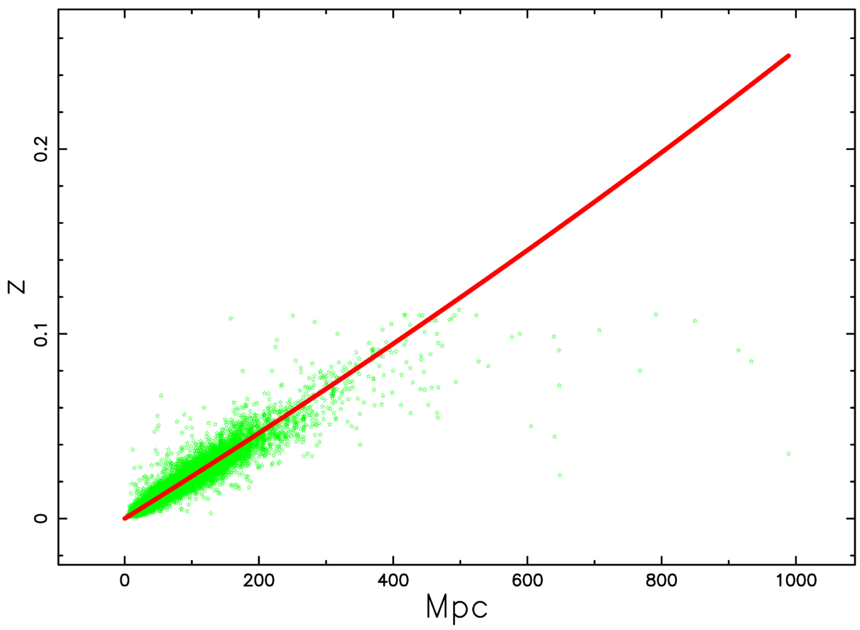

Figure 2. Redshift versus distance for galaxies, green points, and fitted red line with uncertainty.

Table 1. Numerical values of the cosmological parameters for the NED-D catalog for different models in the data analysis.

model	H_0	$\langle n_e \rangle$ Equation (24)	$\langle n_e \rangle$ Equation (27)	$\langle n_e \rangle$ Equation (31)	kn_e Equation (21)
straight line, without uncertainties	64.24 ± 0.14	2.08×10^{-4}	0.507	2969	6.94×10^{-27}
straight line, with uncertainties	67.76 ± 1.08×10^{-2}	2.2×10^{-4}	0.535	3132	7.32×10^{-27}

The above nonlinear regression can also be processed with the Levenberg-Marquardt method [12], which modifies H_0 with uncertainties from 67.76 km·s^{-1}·Mpc^{-1} to 67.80 km·s^{-1}·Mpc^{-1}. In the NED's data, see **Figure 2**, we note the presence of outliers. The main problem with outlier removal is that it may also introduce a bias in the estimation of H_0 and therefore we processed all the data provided by the catalog.

3. The Photometric Maximum

This section reviews the Schechter's luminosity function for galaxies and the photometric maximum in the number of galaxies versus redshift.

3.1. The Schechter Function

The Schechter function, introduced by [20], provides a useful fit for the LF of galaxies

$$\Phi(L)\mathrm{d}L = \left(\frac{\Phi^*}{L^*}\right)\left(\frac{L}{L^*}\right)^{\alpha} \exp\left(-\frac{L}{L^*}\right)\mathrm{d}L, \tag{34}$$

where α sets the slope for low values of L, L^* is the characteristic luminosity, and Φ^* is the normalization. The equivalent distribution in absolute magnitude is

$$\Phi(M)\mathrm{d}M = 0.921\Phi^* 10^{0.4(\alpha+1)(M^*-M)} \exp\left(-10^{0.4(M^*-M)}\right)\mathrm{d}M, \tag{35}$$

where M^* is the characteristic magnitude as determined from the data. We introduce $H_0 = 100h\,\mathrm{km}\cdot\mathrm{s}^{-1}\cdot\mathrm{Mpc}^{-1}$, with $h=1$ when h is not specified and therefore the scaling with h is $M^* - 5\log_{10} h$ and $\Phi^* h^3 \left[\mathrm{Mpc}^{-3}\right]$.

3.2. The Behaviour of the Schechter Function

Under the hypothesis of spherical symmetry, we use the symbol r for the distance d. The radius r in the pseudo-Euclidean cosmology has the following dependence:

$$r = \frac{zc}{H_0}. \tag{36}$$

The flux of radiation, f, is introduced as

$$f = \frac{L}{4\pi r^2}, \tag{37}$$

and is here expressed in $\frac{L_\odot}{\mathrm{Mpc}^2}$. The joint distribution in distance, r, and flux, f, for the number of galaxies is

$$\frac{\mathrm{d}N}{\mathrm{d}\Omega \mathrm{d}r \mathrm{d}f} = \frac{1}{4\pi}\int_0^\infty 4\pi r^2 \Phi\left(\frac{L}{L^*}\right)\delta\left(f - \frac{L}{4\pi r^2}\right)\mathrm{d}r, \tag{38}$$

were the factor ($\frac{1}{4\pi}$) converts the number density into the density for a solid angle and the Dirac delta function selects the required flux. In the case of the Schechter LF, we have

$$\frac{\mathrm{d}N}{\mathrm{d}\Omega \mathrm{d}z \mathrm{d}f} = 4\pi\left(\frac{c}{H_0}\right)^5 z^4 \Phi\left(\frac{z^2}{z_{crit}^2}\right), \tag{39}$$

where $\mathrm{d}\Omega$, $\mathrm{d}z$, and $\mathrm{d}f$ represent the differential of the solid angle, the red shift, and the flux, respectively, and

$$z_{crit}^2 = \frac{H_0^2 L^*}{4\pi f c^2}, \tag{40}$$

where c denotes the speed of light; CODATA recommends $c = 299792.458\ \mathrm{km \cdot s^{-1}}$. The mean red shift of galaxies with a flux f, see Formula (1.105) in [21], is

$$\langle z(f)\rangle = z_{crit}\frac{\Gamma(3+\alpha)}{\Gamma(5/2+\alpha)}. \tag{41}$$

The number of galaxies in z and f as given by Formula (39) has a maximum at

$$z_{\max}(f) = z_{crit}\sqrt{\alpha+2}. \tag{42}$$

The value of $z_{\max}$ can be determined from the histogram of the observed number of galaxies expressed as a function of z. These two formulae, for $\langle z\rangle$ and $z_{\max}$, have been derived for a fixed value of f, which appears in the definition of z_{crit}; we now analyse the case of all the galaxies with $f_{\min} < f < f_{\max}$. The average value of the number of redshifts with flux lying between $f_{\min}$ and $f_{\max}$ is

$$\langle z(f_{\min}, f_{\max})\rangle = -\frac{0.2115 \mathrm{e}^{0.4605 M_{bol,\odot} - 0.4605 M^*} H_0 \Gamma(\alpha+3)\left(f_{\max}^2 - f_{\min}^2\right)}{\Gamma(\alpha+2.5)\left(\sqrt{f_{\max}} f_{\min}^2 - \sqrt{f_{\min}} f_{\max}^2\right)c}, \tag{43}$$

where $M_{bol,\odot}$ is the bolometric luminosity of reference, which is different for each catalog. In this formula, we have used

$$L^* = 10^{0.4 M_{bol,\odot} - 0.4 M^*}. \tag{44}$$

The number of galaxies with flux lying between $f_{\min}$ and $f_{\max}$ is

$$N(z; f_{\min}, f_{\max}) = \frac{1}{\alpha+1}\left(F^* z^{2+\alpha} H_0^{-3-\alpha} c^{3+\alpha} \pi^{\frac{\alpha}{2}} \left(10^{0.4M_{bol,\odot}-0.4M^*}\right)^{-\frac{\alpha}{2}} 2^{\alpha} \right.$$
$$\times \left(f_{\max}^{\frac{\alpha}{2}} \mathrm{e}^{-\frac{2\pi f_{\max} z^2 c^2}{H_0^2 10^{0.4M_{bol,\odot}-0.4M^*}}} M_{\frac{\alpha}{2},\frac{\alpha}{2}+\frac{1}{2}}\left(\frac{4\pi f_{\max} z^2 c^2}{H_0^2 10^{0.4M_{bol\odot}-0.4M^*}}\right) \right. \quad (45)$$
$$\left.\left. - f_{\min}^{\frac{\alpha}{2}} \mathrm{e}^{-\frac{2\pi f_{\min} z^2 c^2}{H_0^2 10^{0.4M_{bol,\odot}-0.4M^*}}} M_{\frac{\alpha}{2},\frac{\alpha}{2}+\frac{1}{2}}\left(\frac{4\pi f_{\min} z^2 c^2}{H_0^2 10^{0.4M_{bol,\odot}-0.4M^*}}\right)\right)\right),$$

where $M_{\kappa,\mu}(z)$ is the Whittaker function, see [22]. **Table 2** reports the typical parameters of different catalogs.

Figure 3 treats all the observed galaxies of the NED and the theoretical curve with data as in **Table 2**. **Table 3** presents a comparison between theory and observation of $\langle z(f_{\min}, f_{\max})\rangle$ and $\langle z(f_{\min}, f_{\max})\rangle$.

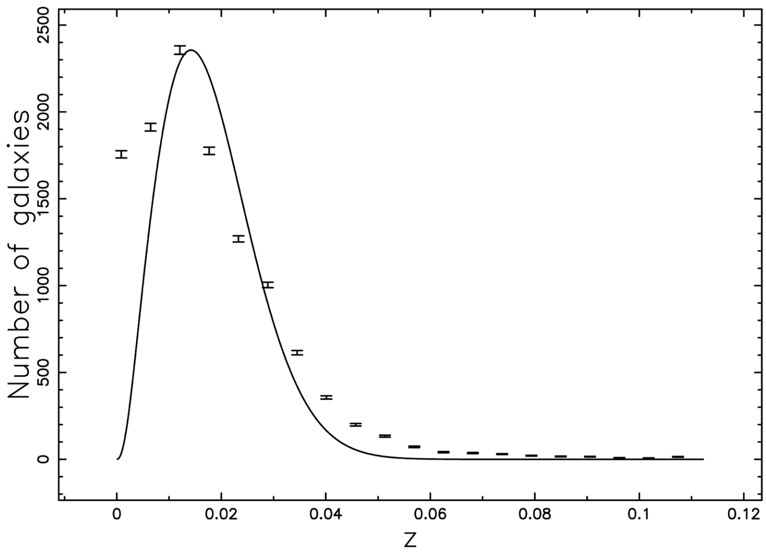

Figure 3. All the galaxies of NED, organized in frequencies versus heliocentric redshift, (empty circles); the error bar is given by the square root of the frequency. The maximum frequency of observed galaxies is at $z = 0.0148$. The full line is the theoretical curve generated by N as given by the application of the Schechter LF which is Equation (45).

Table 2. Catalog, reference and numerical values of α, M^*, $M_{bol,\odot}$, H_0, $f_{\min}$ and $f_{\max}$.

Catalog	reference	α	M^*	M_{bol}	H_0	$f_{\min}$	$f_{\max}$
2dFGRS	[23]	−1.19	−19.79	4.74	100	904	286807
6dF	[23]	−1.19	−19.79	4.74	100	402	6804408
zCOSMOS	[24]	−1.07	−20.1	4.08	69.6	8.97	31787
SDSS DR 12	[25]	−0.9	−30	6.39	69.81	2.39×10^{-2}	7.32×10^{10}
NED	here	−0.9	−22.05	4.74	67	5×10^5	2×10^7

Table 3. Theoretical and observed $\left\langle z\left(f_{\min}, f_{\max}\right)\right\rangle$ and $z_{\max}\left(f_{\min}, f_{\max}\right)$ for the NED catalog.

quantity	observed	theoretical
$\left\langle z\left(f_{\min}, f_{\max}\right)\right\rangle$	0.0202	0.0179
$z_{\max}\left(f_{\min}, f_{\max}\right)$	0.0148	0.0142

4. Simple Models for the Spatial Anisotropy

The mechanisms for the redshift here considered require the evaluation of the average density of electrons along the line of sight, which can be computed by

$$\left\langle n_e\right\rangle = \frac{\int_0^D n_e(x)\mathrm{d}x}{D}, \tag{46}$$

where D is the considered distance. The discrete version is

$$\left\langle n_e\right\rangle = \frac{\sum_i n_{e,i} l_i}{\sum_i l_i}, \tag{47}$$

where $n_{e,i}$ and l_i denote the number density of electrons and length for different zones. This will be called the fundamental integral or fundamental sum.

4.1. Anisotropy in the Catalogs

The first catalog to be analysed is the *HST* Key Project, which explored the value of H_0 in all directions of the sky; the data are reported in **Table 1** and **Table 2** of [10]. **Table 4** reports the average, the standard deviation, the weighted mean, the error of the weighted mean, the minimum, $H_{0,\min}$ and the maximum $H_{0,\max}$ computed as in [26] [27]. Asymmetries for H_0 are also found in the CMB dipole direction considering the angular distribution of type Ia supernovae [28] and in quasars and gamma-ray bursts [29]. We then analysed the NED catalog selecting 64 sectors with equal solid angle, and determined H_0 through a straight line without uncertainties, see **Table 4**.

4.2. The Rim Model

The radius of the cosmic voids as given by the Sloan Digital Sky Survey (SDSS) R7, has been modeled by spheres which have average radius

$$\overline{R_V} = \frac{18.23}{h}\text{Mpc}, \tag{48}$$

see [30]. One model for the asymmetric Hubble constant assumes that the galaxies are situated on the thick surface of spheres having thickness t much smaller than the average radius. We suggest that the density of the free electrons follows the previous trend, and therefore

$$\begin{aligned} n_e(r) &= n_0 \ \text{ if } 0 \le r < a \\ n_e(r) &= n_1 \ \text{ if } a \le r < b \\ n_e(r) &= n_0 \ \text{ if } r \ge b \end{aligned} \tag{49}$$

Table 4. The Hubble constant of the *HST* key project.

Entity	Definition	Value HST-project	NED
n	No. of samples	76	64
$\overline{H_0}$	average	76.7 km·s^{-1}·Mpc^{-1}	65.50 km·s^{-1}·Mpc^{-1}
σ	standard deviation	10.57 km·s^{-1}·Mpc^{-1}	2.44 km·s^{-1}·Mpc^{-1}
$H_{0,\max}$	maximum	124.4 km·s^{-1}·Mpc^{-1}	74.16 km·s^{-1}·Mpc^{-1}
$H_{0,\min}$	minimum	54.79 km·s^{-1}·Mpc^{-1}	58.60 km·s^{-1}·Mpc^{-1}
μ	weighted mean	72.09 km·s^{-1}·Mpc^{-1}	65.28 km·s^{-1}·Mpc^{-1}
$\sigma(\mu)$	error of the weighted mean	0.41 km·s^{-1}·Mpc^{-1}	0.122 km·s^{-1}·Mpc^{-1}

where r is the distance from the origin of a Cartesian 3D reference system. This means that the electron density increases from n_0 at the centre of the sphere to n_1 at $r = a$, remains constant up to $r = b$ (the radius of the void), and then decreases again to n_0 outside the sphere. The fundamental integral of the density as given by Equation (46) can be done in the x-direction over the length $D = 2b$ and split into two parts,

Part I, three pieces if $0 \le y < a$

Part II, two pieces if $a \le y < b$

Corresponding to the lines of sight s_1 and s_2 in **Figure 4**. The result of the integral of the average electron density, see (46), is

$$\begin{aligned}\langle n_e\rangle &= \frac{n_0 b - n_0\sqrt{b^2-y^2} + n_1\sqrt{b^2-y^2} - n_1\sqrt{a^2-y^2} + n_0\sqrt{a^2-y^2}}{b} \quad \text{if } 0 \le y < a \\ \langle n_e\rangle &= \frac{n_0 b - n_0\sqrt{b^2-y^2} + n_1\sqrt{b^2-y^2}}{b} \quad \text{if } a \le y < b\end{aligned} \tag{50}$$

The Hubble constant can be obtained from the average electron density by multiplying by a numerical factor, see Equation (28) for the photo-absorption process. **Figure 5** shows the behaviour of Hubble's constant as a function of the observer's position and **Table 5**, the statistical parameters along the line of sight for this first model.

4.3. The Cord

The starting point is a probability density function (PDF) for the diameter of the astrophysical region, $F(x)$, where x indicates the diameter. The probability, $G(x)\mathrm{d}x$, that a sphere having diameter between x and $x + \mathrm{d}x$ intersects a random line is proportional to their cross section

$$G(x)\mathrm{d}x = \frac{\frac{\pi}{4}x^2 F(x)\mathrm{d}x}{\int_0^\infty \frac{\pi}{4}x^2 F(x)\mathrm{d}x} = \frac{x^2 F(x)\mathrm{d}x}{\langle x^2\rangle}. \tag{51}$$

Given a line which intersects a sphere of diameter x, the probability that the distance from the centre lies in the range $r, r + \mathrm{d}r$ is

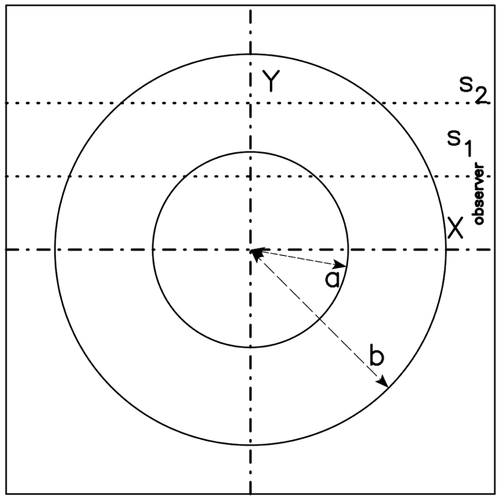

Figure 4. The two circles (sections of spheres) which include the region with an enhancement in electron density are represented by full lines. The observer is situated along the *x* direction, and two lines of sight are indicated.

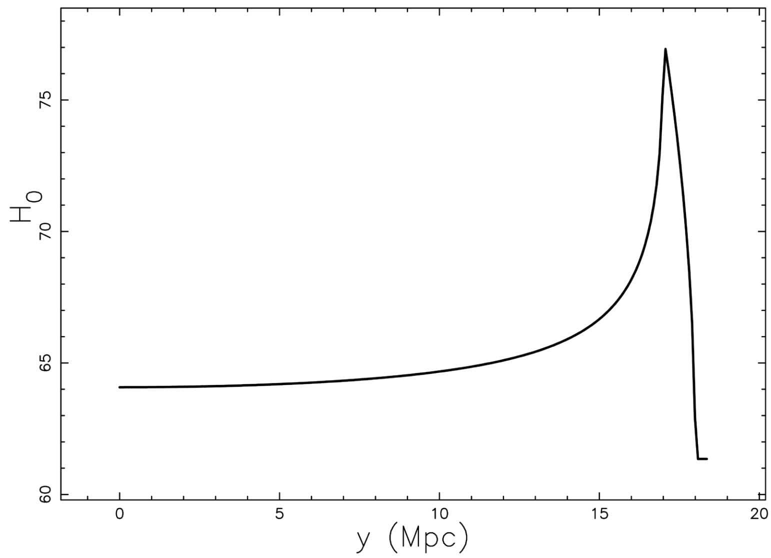

Figure 5. Value of H_0 in the rim model for the photo-absorption process as function of the position; $b = 18$ Mpc, $a = 17$ Mpc, $n_0 = 4.85 \times 10^{-7}$ particles cm^{-3}, and $n_1 = 8.72 \times 10^{-7}$ particles cm^{-3}.

Table 5. The Hubble constant for the photo-absorption process in the rim model.

Entity	Definition	Value
N	No. of samples	200
$\overline{H_0}$	average	65.41 km·s^{-1}·Mpc^{-1}
σ	standard deviation	2.47 km·s^{-1}·Mpc^{-1}
$H_{0,\max}$	maximum	76.93 km·s^{-1}·Mpc^{-1}
$H_{0,\min}$	minimum	61.35 km·s^{-1}·Mpc^{-1}

$$p(r) = \frac{2\pi r \mathrm{d}r}{\frac{\pi}{4}x^2}, \tag{52}$$

and the length of the chord is

$$l = \sqrt{x^2 - 4r^2}, \tag{53}$$

see **Figure 6**.

The probability that spheres in the range $(x, x + \mathrm{d}x)$ are intersected to produce chords with lengths in the range $(l, l + \mathrm{d}l)$ is

$$G(x)\mathrm{d}x \frac{2l\mathrm{d}l}{x^2} = \frac{2l\mathrm{d}l}{\langle x^2 \rangle} F(x)\mathrm{d}x. \tag{54}$$

The probability of having a chord with length between $(l, l + \mathrm{d}l)$ is

$$g(l) = \frac{2l}{\langle x^2 \rangle} \int_l^\infty F(x)\mathrm{d}x. \tag{55}$$

The previous demonstration has been adapted from [31]. A test of the previous integral can be done by inserting as a distribution for the diameters a Dirac delta function

$$F(x) = \delta(x - 2R). \tag{56}$$

As a consequence, the following PDF for chords is obtained:

$$g(l) = \frac{1}{2} \frac{l}{R^2}, \tag{57}$$

which has an average value

$$\langle l \rangle = \frac{4}{3} R, \tag{58}$$

and a variance

$$\sigma^2 = \frac{2R^2}{9}. \tag{59}$$

The distribution function, DF, for equal diameter spheres is

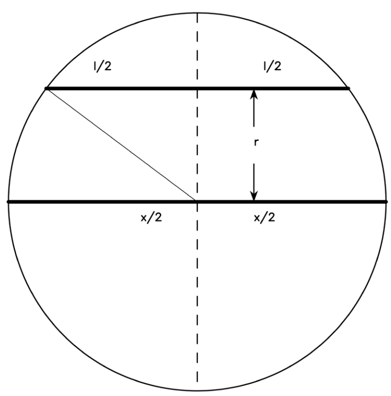

Figure 6. The section having diameter x of the intersected sphere. The chord is drawn with the thicker line and marked with l; the distance between the chord and the centre is r.

$$G(l) = \frac{l^2}{4R^2}, \tag{60}$$

and the random generation of the variate is obtained from the formula

$$l = 2\sqrt{U}R, \tag{61}$$

where U the unit rectangular variate.

Another model for the asymmetric Hubble constant assumes that

1) The light travels a void and the chord is evaluated with Equation (61) where the radius is R_v and the number density n_0.

2) After the void, the light intercepts the halo of a galaxy characterized by a radius R_h and density n_1. The length of the chord is evaluated with Equation (61).

3) The process restarts from (1) and the two chords are different.

The average density is evaluated with Formula (47) and **Table 6** presents the results for the asymmetric Hubble constant in this second model.

5. Voronoi's Models for the Spatial Anisotropy

The faces of the Voronoi Polyhedra share the same property: they are equally distant from two nuclei or seeds. The intersection between a plane and these faces produces diagrams that are similar to the displacement of the edges in 2D Voronoi diagrams. From the point of view of the observations, it is very useful to study the intersection between a slice which crosses the centre of a box and the faces of the irregular polyhedra where the galaxies presumably reside. According to the nomenclature of [32], this cut is classified as $V_P(2,3)$. The parameters that will be used in the following are the kind of nuclei, which can be Poissonian or not Poissonian, the number of nuclei, and the *side* of the box in Mpc. These are used to build the diagrams, see [33]. In order to calibrate the model, the average radius of the voids should be $R_v = 18.23h^{-1}$ Mpc. The density of free electrons can be found by: 1) computing the distance d of a 3D grid point from the nearest face, 2) inserting such a distance in the following piecewise function for the number density of electrons

Table 6. The asymmetric Hubble constant for the second model when $R_v = 18.23$ Mpc, $R_h = 5$ Mpc, $n_0 = 2.8 \times 10^{-7}$ particles cm^{-3}, and $n_1 = 1.4 \times 10^{-6}$ particles cm^{-3}.

Entity	Definition	Value
N	No. of samples	10
$\overline{H_0}$	average	67.13 km·s^{-1}·Mpc^{-1}
σ	standard deviation	1.22 km·s^{-1}·Mpc^{-1}
$H_{0,\max}$	maximum	68.77 km·s^{-1}·Mpc^{-1}
$H_{0,\min}$	minimum	65.26 km·s^{-1}·Mpc^{-1}

$$n_e(d) = n_1 \text{ if } d < c$$
$$n_e(d) = n_0 \text{ if } d \geq c \tag{62}$$

In 2D **Figure 7** shows the behaviour of the number density of electrons that follows the $V_P(2,3)$ behaviour; the parameters of the simulation are presented in **Table 7**. **Figure 8** presents the behaviour of the Hubble constant when the position of the observer varies progressively from left to right. **Table 8** presents the statistics for H_0 in the *third* model.

In 3D the contours of H_0 in Mollweide projection can be drawn when the observer is at the centre of the box, see **Figure 9**; **Table 9** gives the statistics of the Hubble constant for the fourth model.

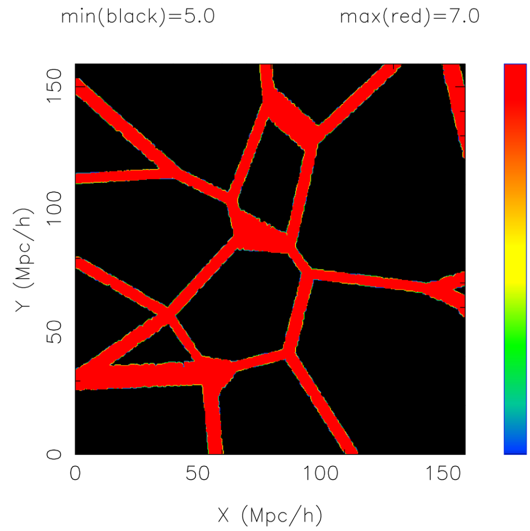

Figure 7. Behaviour of the number density in 10^{-7} particles cm^{-3} for the intersection, $V_P(2,3)$, between a plane and the Voronoi faces.

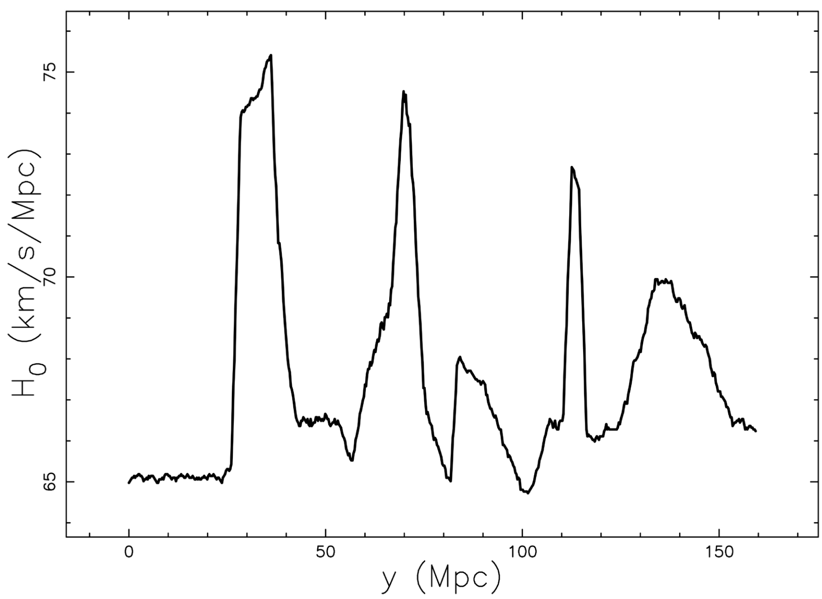

Figure 8. Behaviour of H_0 along different lines of sight.

Table 7. Numerical values for the parameters of the voronoi diagrams.

catalog	Cosmology	type of seeds	seeds	side of box [Mpc]	H_0 (km·s^{-1}·Mpc^{-1})	n_0 (particles cm^{-3})	n_1 (particles cm^{-3})
NED	pseudo-Euclidean	Poissonian	30	441	67	5.0×10^{-7}	5.0×10^{-7}

Table 8. The Hubble constant for $V_P(2,3)$ for different lines of sight, *third* model.

entity	definition	value
N	No. of samples	601
$\overline{H_0}$	average	67.59 km·s^{-1}·Mpc^{-1}
σ	standard deviation	2.61 km·s^{-1}·Mpc^{-1}
$H_{0,\max}$	maximum	75.41 km·s^{-1}·Mpc^{-1}
$H_{0,\min}$	minimum	64.72 km·s^{-1}·Mpc^{-1}

Table 9. The Hubble constant in 3D for different lines of sight in the fourth model.

entity	definition	value
N	No. of samples	4×10^6
$\overline{H_0}$	average	67.21 km·s^{-1}·Mpc^{-1}
σ	standard deviation	3.15 km·s^{-1}·Mpc^{-1}
$H_{0,\max}$	maximum	72.86 km·s^{-1}·Mpc^{-1}
$H_{0,\min}$	minimum	61.38 km·s^{-1}·Mpc^{-1}

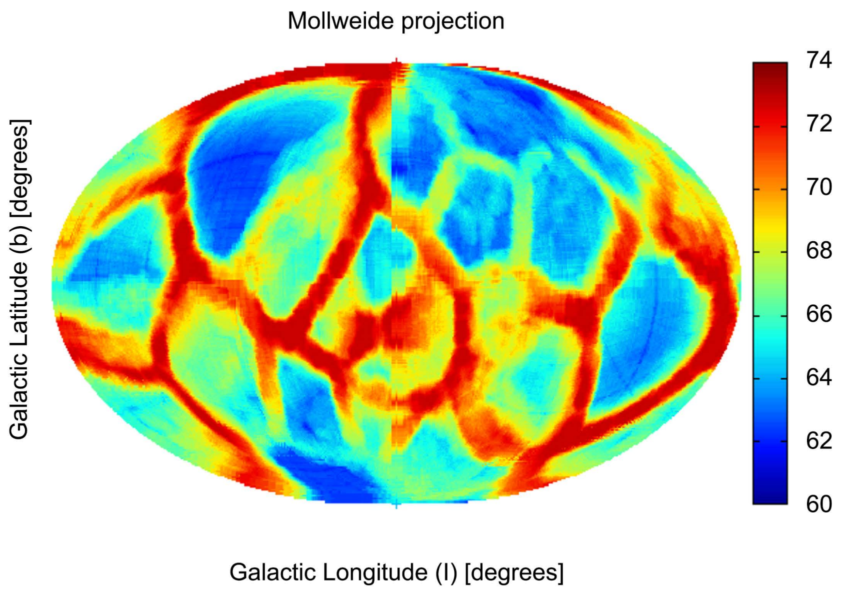

Figure 9. False color contour plot of H_0 as given by the Voronoi's diagram in the Mollweide map in galactic coordinates with the Galactic center in the middle, parameters as in Table 7.

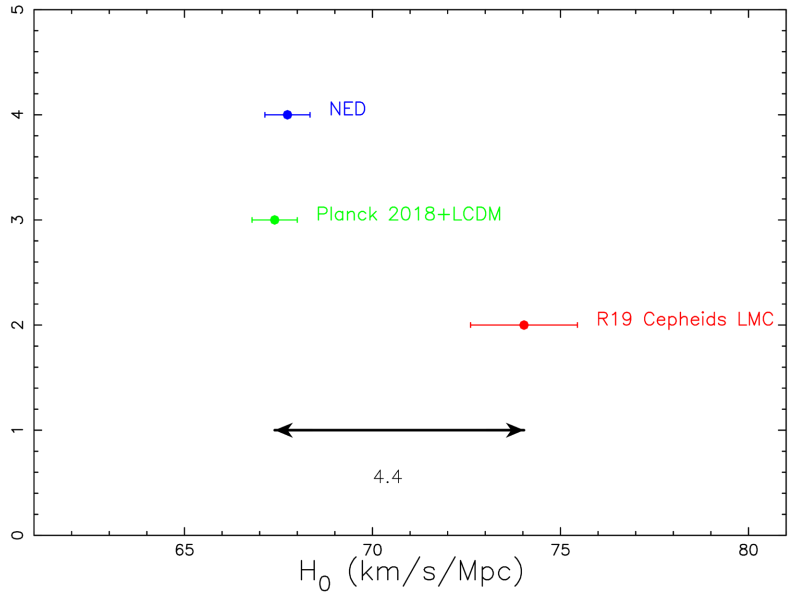

Figure 10. The present tension on H_0 (black line with two arrows) and our result in the case of the NED sample (blue line).

6. Conclusions

Anomalous redshift

We revitalized the Beer-Lambert law which allows deriving an expression for the redshift as a function of the number density of electrons, see Equation (16). We reviewed three physical mechanisms which produce a definition of the Hubble constant as a function of the number density of electrons, namely, a plasma effect, see Equation (25), an NTL approach, see Equation (28) and the interaction of an electromagnetic wave with an electron, see Equation (33).

Values of H_0

The Hubble constant as determined by processing the NED's galaxies, turns out to be $H_0 = (64.24 \pm 0.14)\,\mathrm{km}\cdot\mathrm{s}^{-1}\cdot\mathrm{Mpc}^{-1}$ in the case of a fit with a straight line without uncertainties and $H_0 = (67.76 \pm 0.01)\,\mathrm{km}\cdot\mathrm{s}^{-1}\cdot\mathrm{Mpc}^{-1}$ in the case of a fit with a straight line with uncertainties, see Table 1. The weighted mean with the standard deviation as error is

$$\overline{H_0} = (67.74 \pm 2.49)\,\mathrm{km}\cdot\mathrm{s}^{-1}\cdot\mathrm{Mpc}^{-1} \quad \text{Ned-catalog.} \tag{63}$$

Figure 10 presents the values of reference for H_0 and the value here derived.

Anisotropy

The problem of the anisotropy in the Hubble constant has been explained by four methods, which require an increase in the number density of relativistic electrons in the intergalactic medium around the clusters of galaxies, see Table 5, Table 6, Table 8 and Table 9. These models agree with the revised version of the cosmological principle suggested in 2012 in [34]: "The galaxies, as well our galaxy, are situated on the faces of a Voronoi polyhedron. The spatial distribution of galaxies will follow approximately the geometrical rules as well the standard photometric rules."

Conflicts of Interest

The author declares no conflicts of interest regarding the publication of this paper.

References

[1] Planck Collaboration, Aghanim, N., Akrami, Y., *et al.* (2018) Planck 2018 Results. VI. Cosmological Parameters.

[2] Riess, A.G., Casertano, S., Yuan, W., Macri, L.M. and Scolnic, D. (2019) Large Magellanic Cloud Cepheid Standards Provide a 1% Foundation for the Determination of the Hubble Constant and Stronger Evidence for Physics beyond ΛCDM. *The Astrophysical Journal*, **876**, 85. https://doi.org/10.3847/1538-4357/ab1422

[3] Hart, L. and Chluba, J. (2022) Varying Fundamental Constants Principal Component Analysis: Additional Hints about the Hubble Tension *MNRAS*, **510**, 2206-2227. https://doi.org/10.1093/mnras/stab2777

[4] Wojtak, R. and Hjorth, J. (2022) Intrinsic Tension in the Supernova Sector of the Local Hubble Constant Measurement and Its Implications *MNRAS*, **515**, 2790-2799. https://doi.org/10.1093/mnras/stac1878

[5] Mostaghel, N. (2022) The Source of Tension in the Measurements of the Hubble Constant. *International Journal of Astronomy and Astrophysics*, **12**, 273-280. https://doi.org/10.4236/ijaa.2022.123016

[6] Le Denmat, G. and Vigier, J.P. (1975) Les supernovae de type I et l'anisotropie de la "constante" de Hubble. *Academie des Sciences Paris Comptes Rendus Serie B Sciences Physiques*, **280**, 459.

[7] Karoji, H. and Moles, M. (1975) Les galaxies de Markarian et l'anisotropie angulaire de la "constante" de Hubble. *Academie des Sciences Paris Comptes Rendus Serie B Sciences Physiques*, **280**, 609.

[8] Wang, Y., Spergel, D.N. and Turner, E.L. (1998) Implications of Cosmic Microwave Background Anisotropies for Large-Scale Variations in Hubble's Constant. *The Astrophysical Journal*, **498**, 1. https://doi.org/10.1086/305539

[9] Schwarz, D.J. and Weinhorst, B. (2007) (An)isotropy of the Hubble Diagram: Comparing Hemispheres *A&A*, **474**, 717-729. https://doi.org/10.1051/0004-6361:20077998

[10] McClure, M.L. and Dyer, C.C. (2007) Anisotropy in the Hubble Constant as Observed in the HST Extragalactic Distance Scale Key Project Results *New Astronomy*, **12**, 533-543. https://doi.org/10.1016/j.newast.2007.03.005

[11] Kragh, H. (2017) Is the Universe Expanding? Fritz Zwicky and Early Tired-Light Hypotheses. *Journal of Astronomical History and Heritage*, **20**, 2-12. https://doi.org/10.3724/SP.J.1440-2807.2017.01.01

[12] Press, W.H., Teukolsky, S.A., Vetterling, W.T. and Flannery, B.P. (1992) Numerical Recipes in FORTRAN. The Art of Scientific Computing. Cambridge University Press, Cambridge.

[13] Lambert, J.H. (1760) Photometria sive de mensura et gradibus luminis, colorum et umbrae. Sumptibus vidvae E. Klett, typis CP Detleffsen.

[14] Beer, A. (1852) Bestimmung der absorption des rothen lichts in farbigen flussigkeiten. *Annalen der Physik*, **162**, 78-88. https://doi.org/10.1002/andp.18521620505

[15] Hubble, E. (1929) A Relation between Distance and Radial Velocity among Extra-Galactic Nebulae. *Proceedings of the National Academy of Science*, **15**, 168.

https://doi.org/10.1073/pnas.15.3.168

[16] Brynjolfsson, A. (2004) Redshift of Photons Penetrating a Hot Plasma.

[17] Brynjolfsson, A. (2009) Plasma-Redshift Cosmology: A Review. 2*nd Crisis in Cosmology Conference* (*Astronomical Society of the Pacific*), Vol. 413, 169-189.

[18] Ashmore, L.E. (2022) Data from 14,577 Cosmological Objects and 14 FRBS Confirm the Predictions of New Tired Light (NTL) and Lead to a New Model of the IGM. *Journal of Physics*: *Conference Series*, **2197**, Article ID: 012003. https://doi.org/10.1088/1742-6596/2197/1/012003

[19] Weidner, H. (2014) Limb Redshift of the Fraunhofer Lines in the Solar Spectrum.

[20] Schechter, P. (1976) An Analytic Expression for the Luminosity Function for Galaxies. *The Astrophysical Journal*, **203**, 297. https://doi.org/10.1086/154079

[21] Padmanabhan, T. (1996) Cosmology and Astrophysics through Problems. Cambridge University Press, Cambridge.

[22] Olver, F.W.J., Lozier, D.W., Boisvert, R.F. and Clark, C.W. (2010) NIST Handbook of Mathematical Functions. Cambridge University Press, Cambridge.

[23] Zaninetti, L. (2014) A Near Infrared Test for Two Recent Luminosity Functions for Galaxies. *Revista Mexicana de Astronomia y Astrofisica*, **50**, 7-14.

[24] Zaninetti, L. (2015) On the Number of Galaxies at High Redshift. *Galaxies*, **3**, 129-155. https://doi.org/10.3390/galaxies3030129

[25] Zaninetti, L. (2018) The Great Wall of SDSS Galaxies. *International Journal of Astronomy and Astrophysics*, **8**, 258-266. https://doi.org/10.4236/ijaa.2018.83018

[26] Leo, W.R. (1994) Techniques for Nuclear and Particle Physics Experiments. Springer, Berlin. https://doi.org/10.1007/978-3-642-57920-2

[27] Zaninetti, L. (2010) New Formulas for the Hubble Constant in a Euclidean Static Universe. *Physics Essays*, **23**, 298. https://doi.org/10.4006/1.3386219

[28] Krishnan, C., Mohayaee, R., Colgáin, E.Ó., Sheikh-Jabbari, M.M. and Yin, L. (2022) Hints of FLRW Breakdown from Supernovae. *Physical Review D*, **105**, Article ID: 063514. https://doi.org/10.1103/PhysRevD.105.063514

[29] Luongo, O., Muccino, M., Colgáin, E.O., Sheikh-Jabbari, M.M. and Yin, L. (2022) Larger H_0 Values in the CMB Dipole Direction. *Physical Review D*, **105**, Article ID: 103510. https://doi.org/10.1103/PhysRevD.105.103510

[30] Pan, D.C., Vogeley, M.S., Hoyle, F., Choi, Y.Y. and Park, C. (2012) Cosmic Voids in Sloan Digital Sky Survey Data Release 7. *MNRAS*, **421**, 926-934. https://doi.org/10.1111/j.1365-2966.2011.20197.x

[31] Ruan, J.Z., Litt, M.H. and Krieger, I.M. (1988) Pore Size Distributions of Foams from Chord Distributions of Random Lines: Mathematical Inversion and Computer Simulation. *Journal of Colloid and Interface Science*, **126**, 93-100. https://doi.org/10.1016/0021-9797(88)90103-8

[32] Okabe, A., Boots, B., Sugihara, K. and Chiu, S. (2000) Spatial Tessellations. Concepts and Applications of Voronoi Diagrams. 2nd Edition, Wiley, Chichester, New York. https://doi.org/10.1002/9780470317013

[33] Zaninetti, L. (1991) Dynamical Voronoi Tessellation. III—The Distribution of Galaxies. *A&A*, **246**, 291-300.

[34] Zaninetti, L. (2012) Revisiting the Cosmological Principle in a Cellular Framework. *Journal of Astrophysics and Astronomy*, **33**, 399-416. https://doi.org/10.1007/s12036-012-9155-3